Supporting Information

Heat Dissipation Regulation for Improved Thermal Stability and Efficiency of Planar Perovskite Solar Cells

Jingyao Feng [a]†, Wenda Shi [b]†, Xin Wang [a]*, Hui Wang [c], Yanan Wang [d], Hongwei Zhang[a], Lina Wang[a], Yuchen Song[a], Ziyu Liu [b], Pei Liu [b], Xueling Zhao [a], Wenqin Li [a], Lifei Chen [a]*, Xiaoming Zhao [e]*

Affiliations:

[a] School of Energy and Materials, Shanghai Engineering Research Center of Advanced Thermal Functional Materials, Shanghai Thermophysical Properties Big Data Professional Technical Service Platform, Shanghai Polytechnic University, Shanghai 201209, China.

[b]School of Chemistry and Chemical Engineering, Northwestern Polytechnical University, Xi'an, P. R. China.

[c] Shanghai Research Institute of Materials Co. Ltd. Shanghai, 200437, China.

[d] College of Mathematics and Physics, Shanghai University of Electric Power, Shanghai, 201306, China.

[e] Institute for Frontier Science, Nanjing University of Aeronautics and Astronautics, Nanjing 210016, China.

E-mail: xinwang@sspu.edu.cn, lfchen@sspu.edu.cn, xiaoming.zhao@nuaa.edu.cn

†The authors contributed equally to this work.

1. Experiment section

1.1 Materials.

All the chemicals were purchased from commercial vendors without further purification. SnO_2 colloid precursor (tin (iv) oxide, 15% in H_2O colloidal dispersion) was purchased from Alfa Aesar. Dimethylformamide (DMF), Dimethyl sulfoxide (DMSO), Acetonitrile (AN), Isopropanol (IPA), and Chlorobenzene (CB) were purchased from Sigma-Aldrich; Lead iodine (PbI_2), Formamidinium iodide (FAI), Methylammonium iodide (MAI), Methylammonium chloride (MACl), 2,2',7,7'-Tetrakis [N, N-di(4-methoxyphenyl)amino]-9,9'-spirobifluorene (Spiro-OMe

TAD) were all purchased from Xi'an Yuri Solar Co., Ltd.

1.2 Synthesis of 2D g-C_3N_4:

The carbon nitride material g-C_3N_4 was prepared using the heat shrinkage polymerization method, which uses melamine as the raw material. Weight 10g melamine in a porcelain ark and put into a tube furnace, nitrogen gas is introduced to heat up to 550 °C at 2.5 °C/min, and holding at 550 °C for 4 hours, the reaction product bulk g-C_3N_4 is obtained after natural cooling down to room temperature and grinding in a mortar. Then, the bulk g-C_3N_4 powder was put into the muffle furnace, heated to 500 °C at 5 °C/min, kept at 500 °C for 2 hours, and then naturally cooled to room temperature for grinding to obtain the finally g-C_3N_4 nanosheets.

1.3 Precursor Preparation and Device Fabrication

Firstly, g-C_3N_4 (0.1-0.5 mg/ml) was added to deionized water and DMF, respectively, and sonicated for 10 h, after which it was filtered through a filter head with a filtration diameter of 0.45 μm to obtain the precursor solution, which was used to replace the original solvent. Next, SnO_2 nanoparticles were diluted with deionized water to achieve a nanoparticle dispersion with a concentration of 2.67%. For comparative purposes, the markers use pure solvents without adding g-C_3N_4. ITO glass was cleaned sequentially with detergent, deionized water, acetone, and isopropanol (IPA). Before use, the ITO

was cleaned with ultraviolet ozone for 10 minutes. Then, the substrate was spin-coated with a thin layer of SnO_2 nanoparticle film at 4,000 rpm. for 30 s and annealed in ambient air at 150 °C for 30min. It is better to clean the substrate with ultraviolet ozone for 10 minutes to improve the surface wetting. After that, 1.5M of PbI_2 in DMF: DMSO (9:1) solvent was spin-coated onto SnO_2 at 1,500 rpm. for 30 s, then annealed at 70 °C for 1min, and then cooled to room temperature. For $FAMAPbI_3$ perovskite film deposition, a solution of FAI: MAI: MACl (90mg:6.39mg:9mg in 1ml IPA) was spin-coated onto the PbI_2 at a spin rate of 2,000 rpm. for 30s, followed by thermal annealing at 150 °C for 15min in ambient air conditions (30–40% humidity). Then the hole transporting layer was deposited on top of the perovskite layer at a spin rate of 3,000 rpm. for 30s using 2,2',7,7'-Tetrakis[N, N-di(4-methoxyphenyl)amino]-9,9'-spirobifluorene (Spiro-OMeTAD) solution, which consisted of 72.3mg Spiro-OMeTAD, 17.5µl bis(trifluoromethane) sulfonimide lithium salt (Li-TFSI) stock solution (520mg Li-TFSI in 1ml acetonitrile), 28.8µl 4-tertbutylpyridine and 1ml chlorobenzene. Finally, 100nm of Ag film was thermally evaporated as a counter electrode using a shadow mask. When measuring the device, a 0.08 cm^2 non-reflective mask was used to define the accurate active cell area.

1.4 Characteristics

X-ray diffraction (XRD) measurements are carried out on TCPUI K780 over the range of 2θ = 5−55.0° with a step size of 0.01° and 0.4s per step. UV-Vis-NIR absorption spectra are recorded on Cary 5000 UV-Visible-NIR spectrophotometer. The sample films are deposited on an ITO substrate. Steady-state photoluminescence (PL) and time-resolved photoluminescence (TRPL) are measured using a Spectrofluorometer FS5 (Edinburgh et al.) with excitation at 475 nm. The morphology of perovskite thin films and cross-sectional SEM images were measured using a cold field-emission scanning electron microscope (Hitachi S4800). The thermal images were taken using a FLIR infrared camera (FLIR T540, USA). The thermal diffusivity was measured by LFA 467 HT Hyperflash (Netzsch Germany). The electrochemical impedance spectroscopy (EIS) measurements were determined on an electrochemical workstation RHA-

CHI800D. The current density–voltage (*J–V*) characteristics of the devices were measured using a Keithley 2400 Source Meter under standard AM1.5 G illumination (SolarIV-300A; Zolix, China), and the light intensity was calibrated using a standard silicon reference cell. The *J-V* curves were measured by forward scan (-0.1 to 1.20 V) and reverse scan (1.20 to -0.1 V) at a scanning rate of 100 mV/s (voltage step: 10 mV, delay time: 1 ms).

1.5 Trap density measurement.

The trap-state density N_t of perovskite films with different ETLs was measured by space-charge-limited current (SCLC) method using a diode configuration of ITO/SnO_2/Perovskite/$PC_{61}BM$/Ag for electron by taking the dark current density in the range of 0-4 V and fitting the results to a space-charge-limited form, where the N_t was calculated according to the equation:

$$N_t = \frac{2V_{TFL}\varepsilon_0\varepsilon_r}{eL^2}$$

Where V_{TFL} is the trap-filled limit voltage, ε_0 is the vacuum permittivity (ε_0 =8.8×10^{-12} F m^{-1}), and e is the electron charge (e=1.6×10^{-19} C), L is the thickness of the perovskite film (L=800 nm), and the adopted ε_r is 62.23.

1.6 Electron mobility.

We have measured electron mobility using different ETLs in the same device structure to gain insights into the charge transport. Specifically, the electron-only device was designed and fabricated using an ITO/ETL/Ag structure. In this analysis, we assumed that the current is only related to electrons. When the effects of diffusion and the electric field are neglected, the SCLC can determine the current density. The devices' dark J–V curves were performed on a Keithley 2400 source at ambient conditions. The electron mobility (μ_e) is extracted by fitting the J–V curves using the Mott–Gurney law:

$$\mu_e = \frac{8JL^3}{9\varepsilon_0\varepsilon_r(V_{app} - V_r - V_{bi})^2}$$

Where J is the current density, L is the thickness of different ETLs, ε_0 the vacuum permittivity, ε_r the dielectric permittivity of various ETL, V_{app} is the applied voltage, V_r *is* the voltage loss due to radiative recombination, and V_{bi} the built-in voltage owing to the different work function between the anode and cathode.

1.7 Thermal diffusivity relates

Thermal diffusivity relates to the homogeneous temperature performance of the thermal conductivity process of the material; this parameter is crucial for the analysis of the unsteady thermal conductivity process; the thermal diffusivity definition equation:

$$\alpha = \frac{k}{\rho C}$$

where k is the thermal conductivity, ρ is the density, and C is the specific heat capacity.

2. Supplementary figures

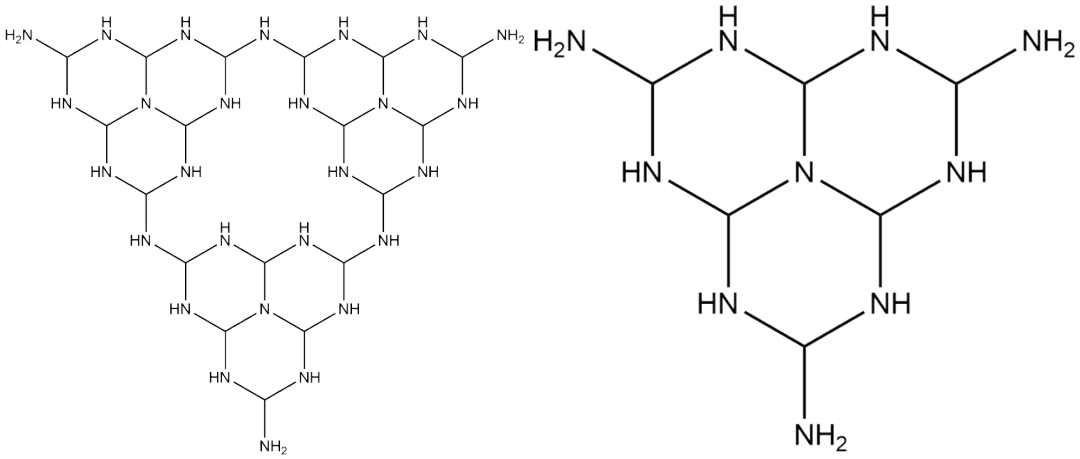

Figure S1. Schematic diagram of g-C_3N_4 structure, with heptazine ring structure (left) and triazine ring structure (right).

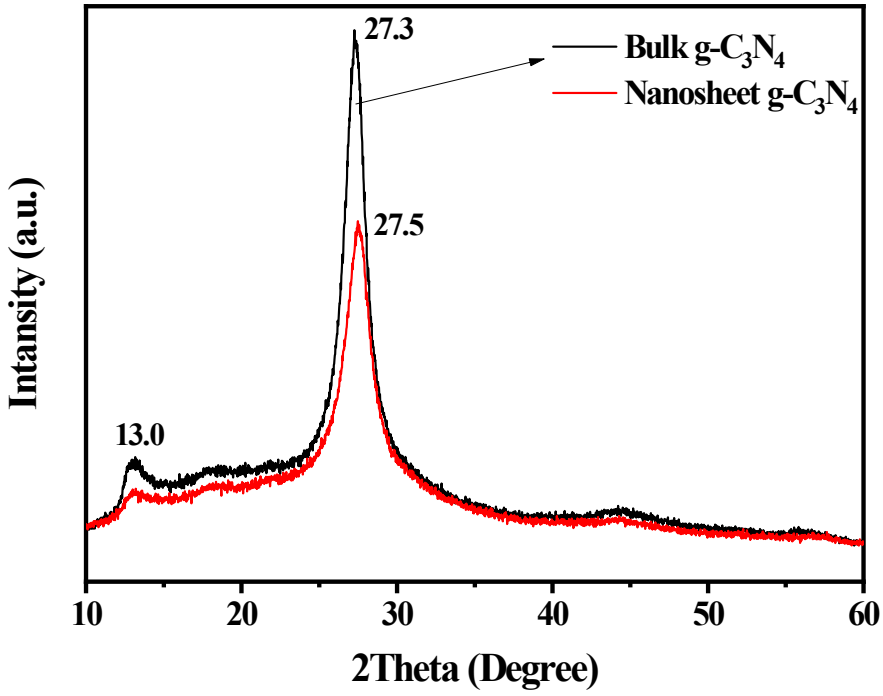

Figure S2. The XRD profile of g-C_3N_4.

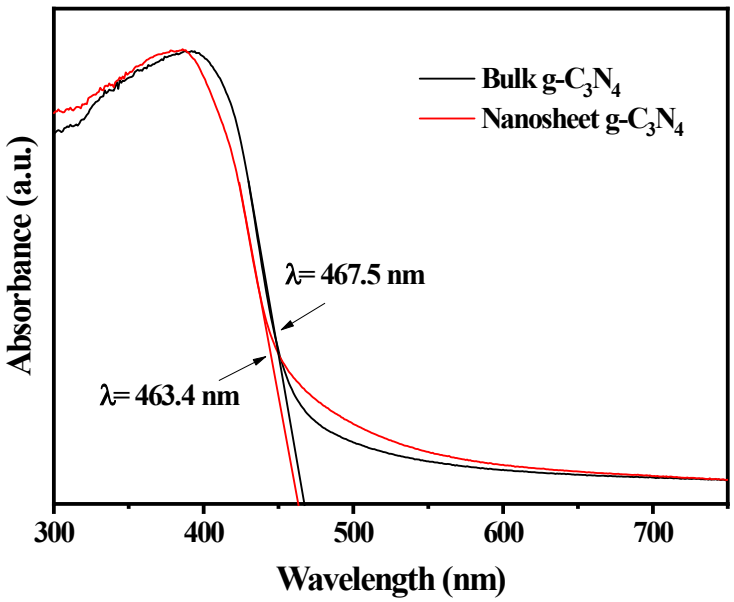

Figure S3. The UV-visible absorption profile of g-C_3N_4.

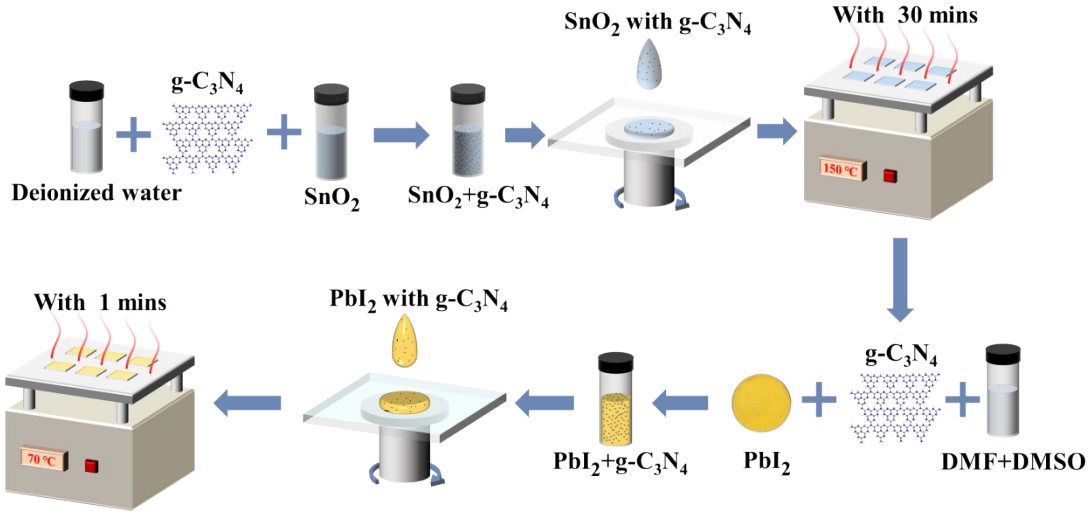

Figure S4. Schematic diagram of the deposition for SnO_2 with g-C_3N_4 layer and perovskite with g-C_3N_4 layer.

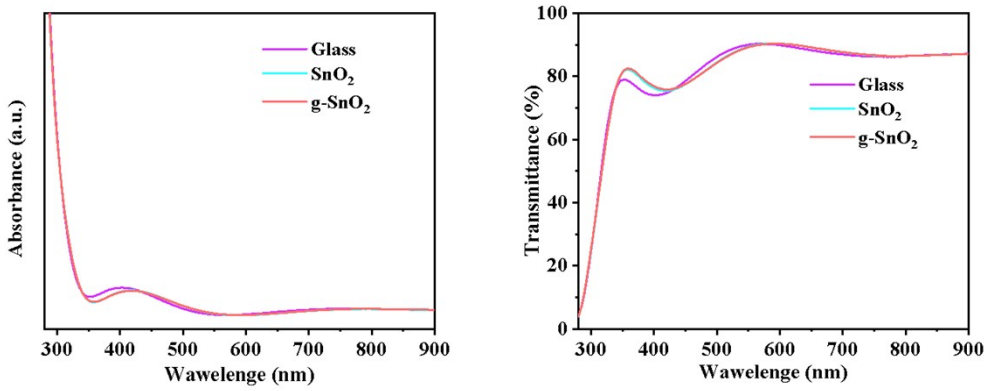

Figure S5. UV-vis absorption spectra SnO_2 and g-SnO_2 films spin-coated on the ITO substrates.

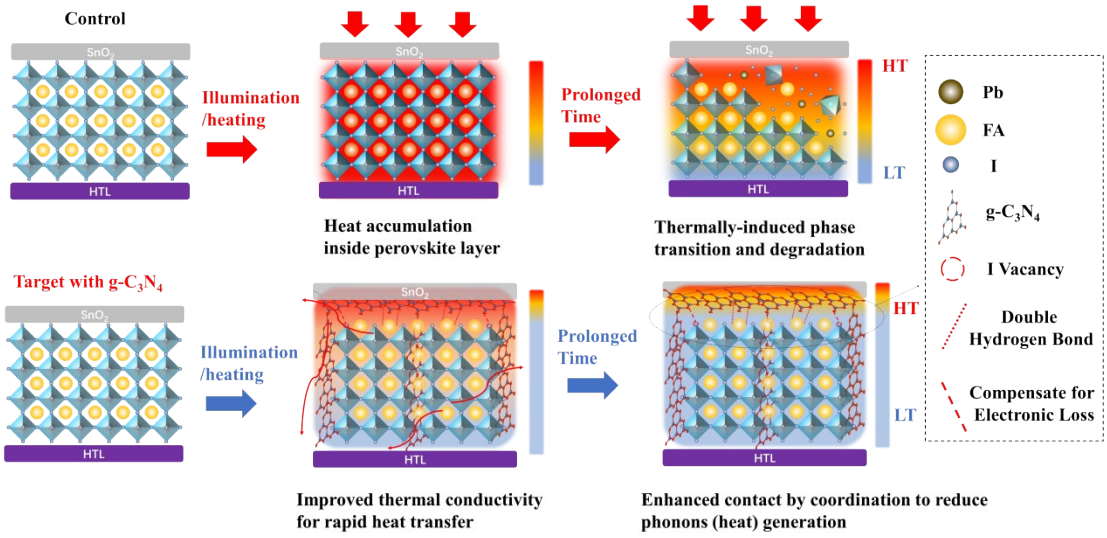

Figure S6. Diagram of the heat dissipation mechanism of g-C_3N_4 as a heat transport channel

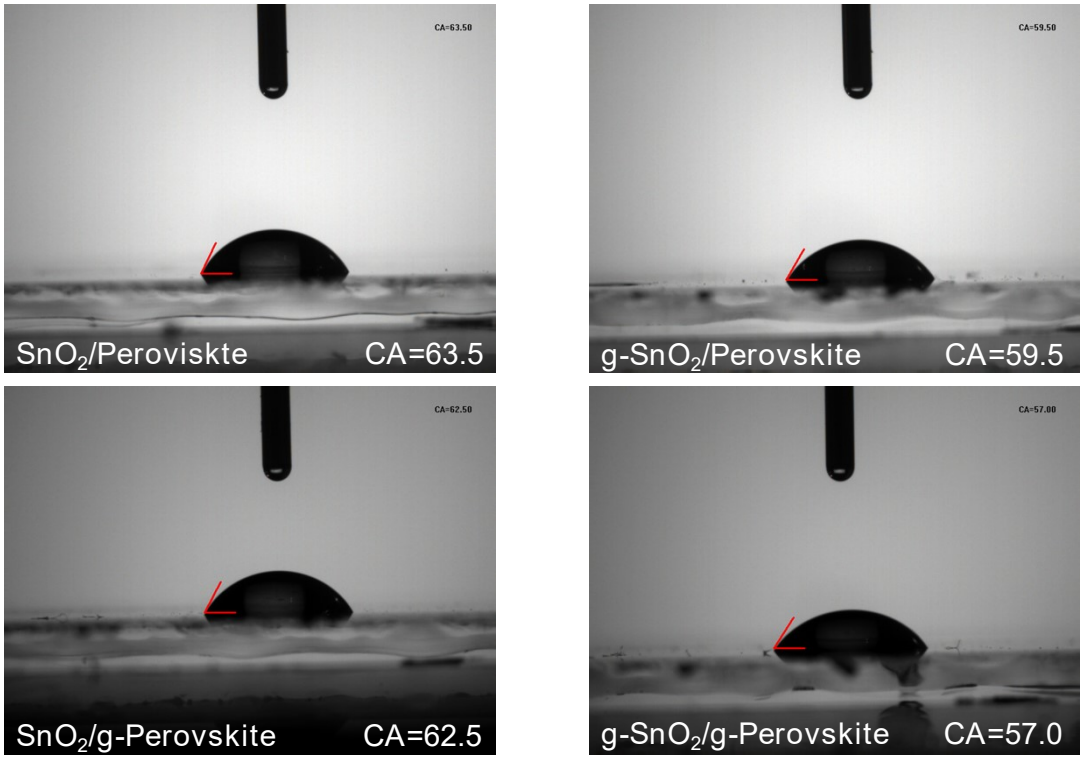

Figure S7. Water droplet contact angles on surfaces, including SnO_2/perovskite, g-SnO_2/perovskite, SnO_2/g-perovskite, and g-SnO_2/g-perovskite.

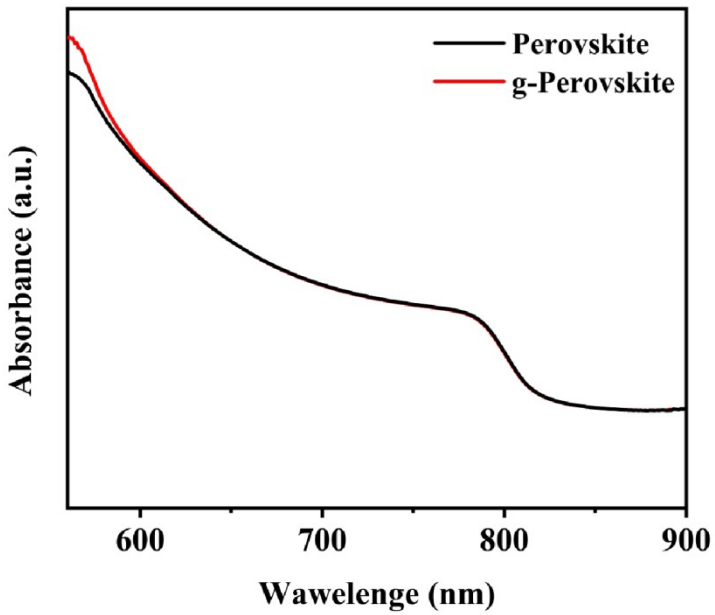

Figure S8. UV-vis absorption spectra Perovskite and g-Perovskite films spin-coated on the ITO substrates.

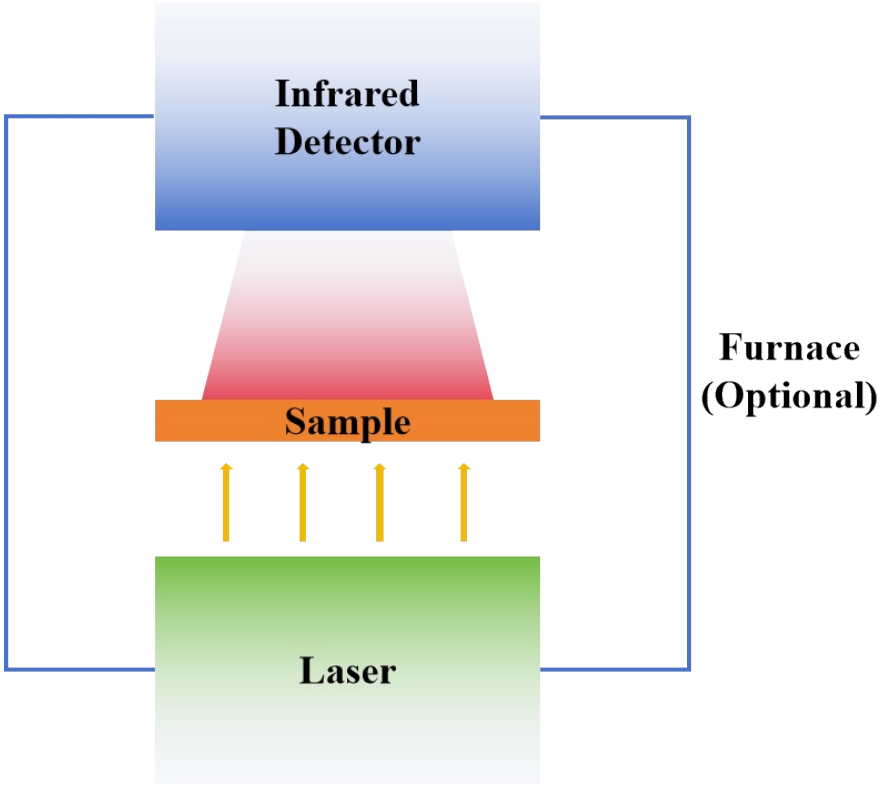

Figure S9. Schematic diagram of the laser thermal conductivity meter.

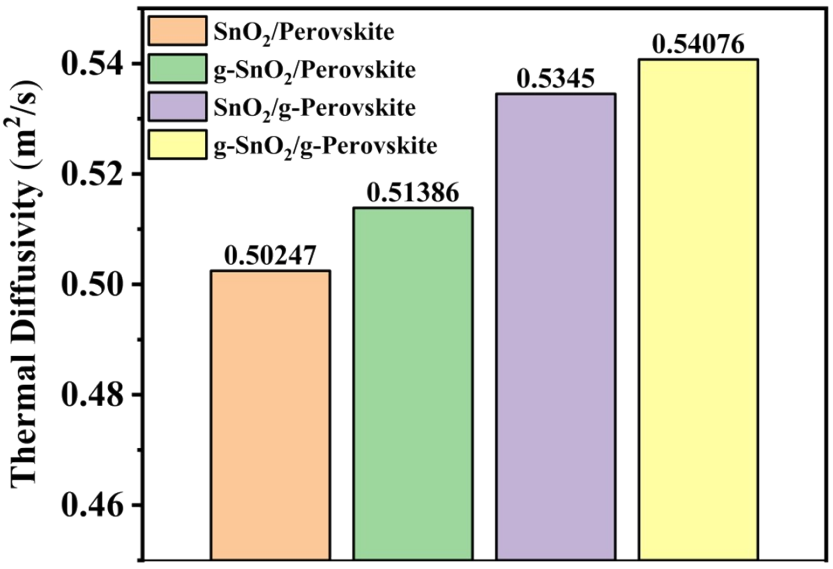

Figure S10. Thermal diffusion coefficients under 50 °C of various films.

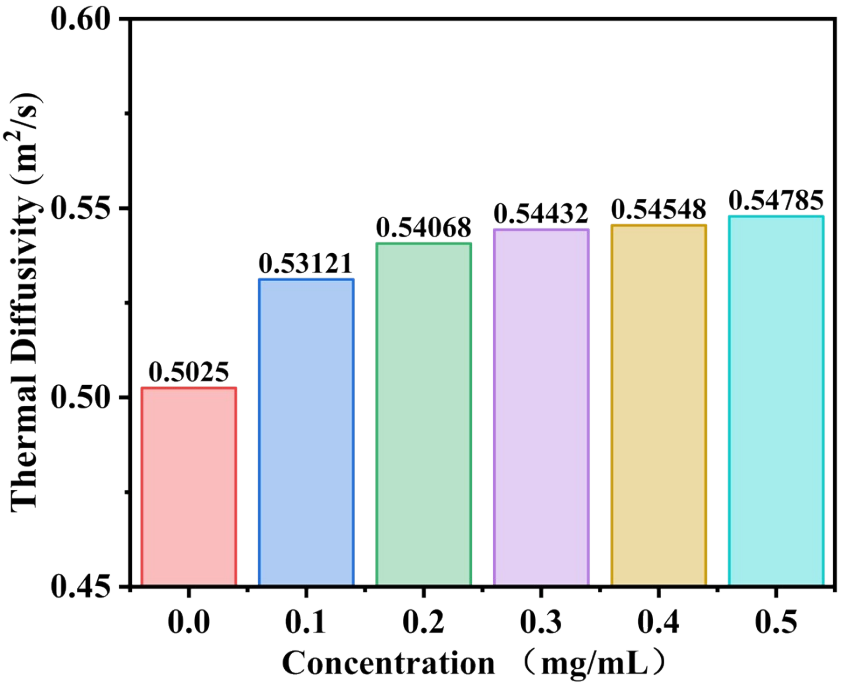

Figure S11. Thermal diffusion coefficients under 50°C of various concentration.

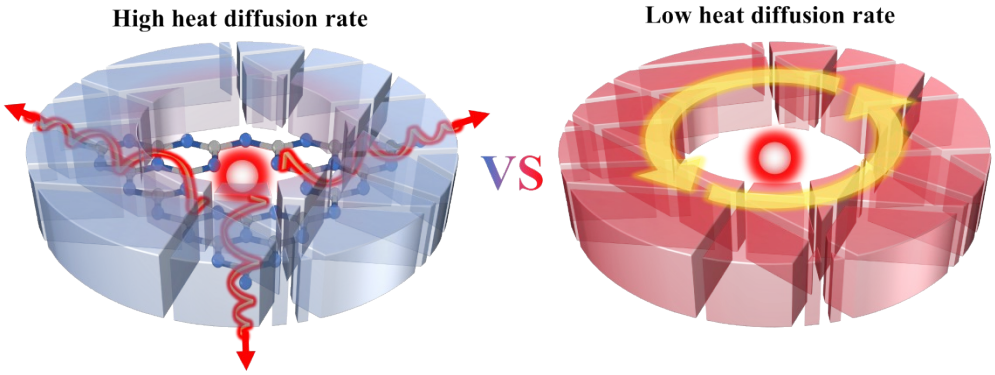

Figure S12. Different heat diffusion rates on PSCs with and without g-C_3N_4 assistance.

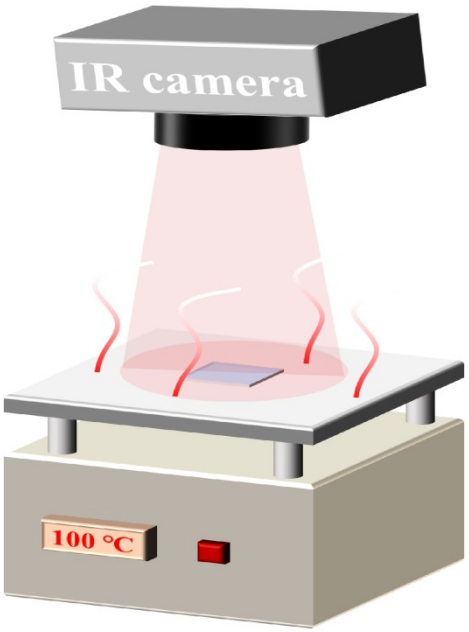

Figure S13. A Schematic representation of the IR thermal images test.

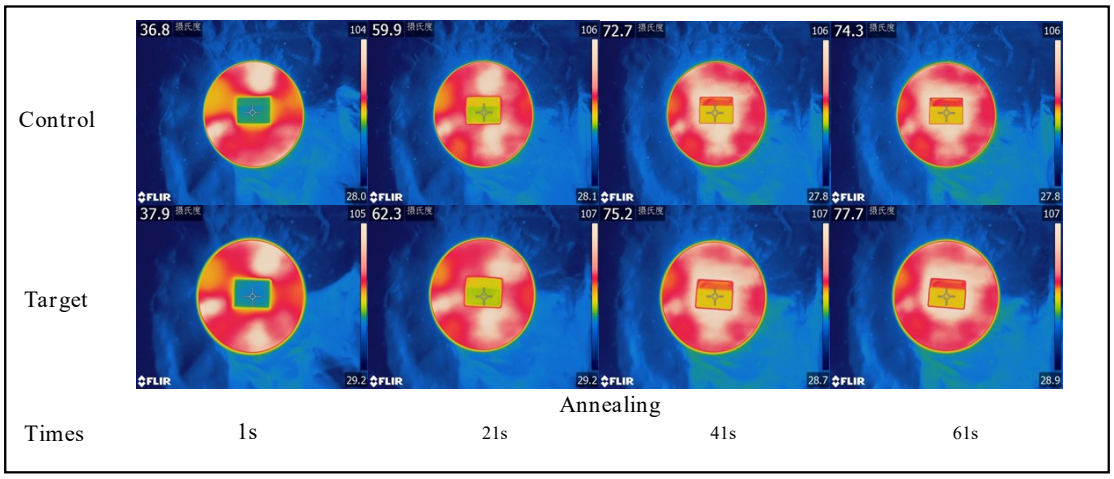

Figure S14. IR thermal images of different films under 100℃ over time. All samples were prepared on the glass substrate.

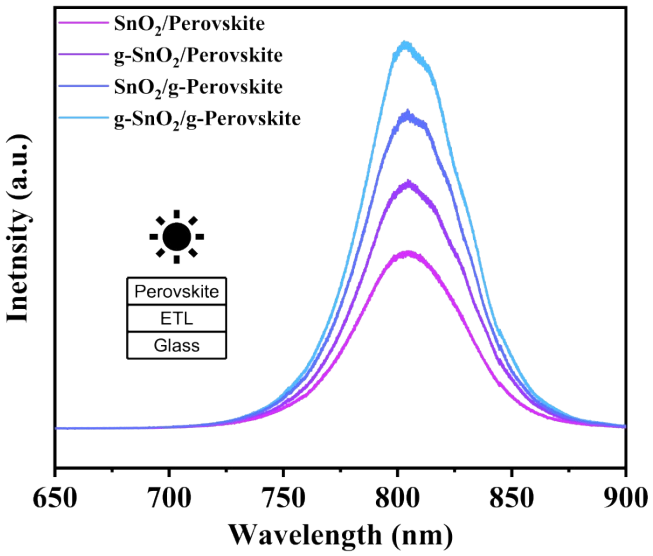

Figure S15. PL spectra of perovskite films, including SnO_2/Perovskite, g-SnO_2/Perovskite, SnO_2/g-Perovskite, and g-SnO_2/g-Perovskite.

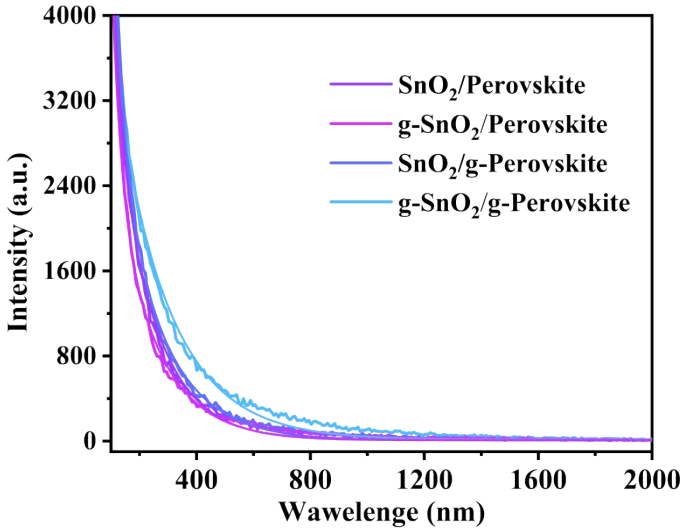

Figure S16. TRPL spectra of perovskite films, including SnO_2/Perovskite, g-SnO_2/Perovskite, SnO_2/g-Perovskite, and g-SnO_2/g-Perovskite.

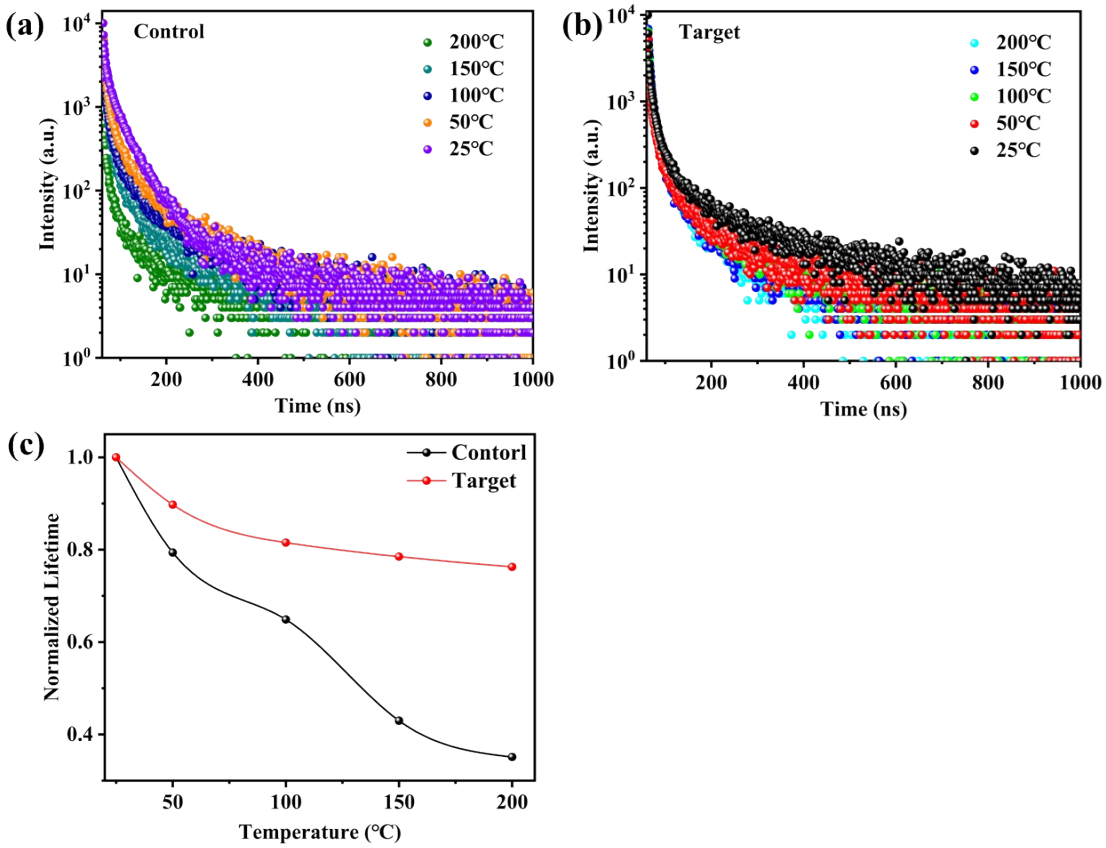

Figure S17. (a,b)TRPL spectra of perovskite films at different temperatures. (c) Trend diagram of the normalized TRPL lifetime.

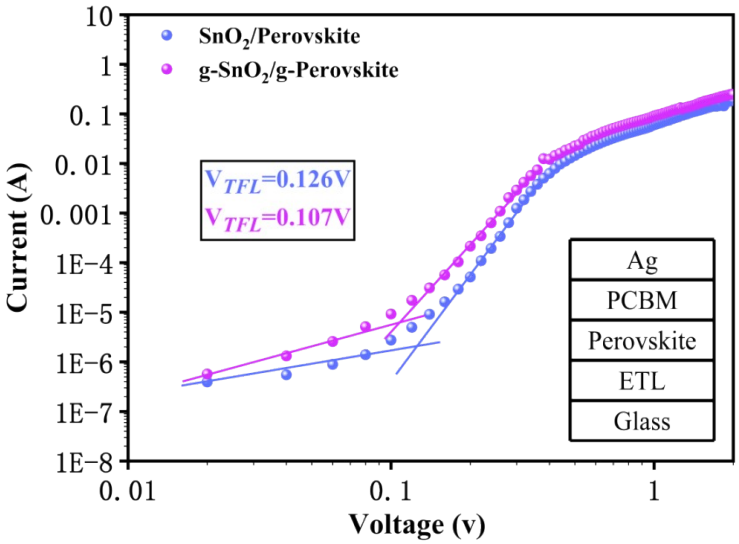

Figure S18. Different $I-V$ curves of electron-only devices in dark, including SnO_2/perovskite and g-SnO_2/g-perovskite.

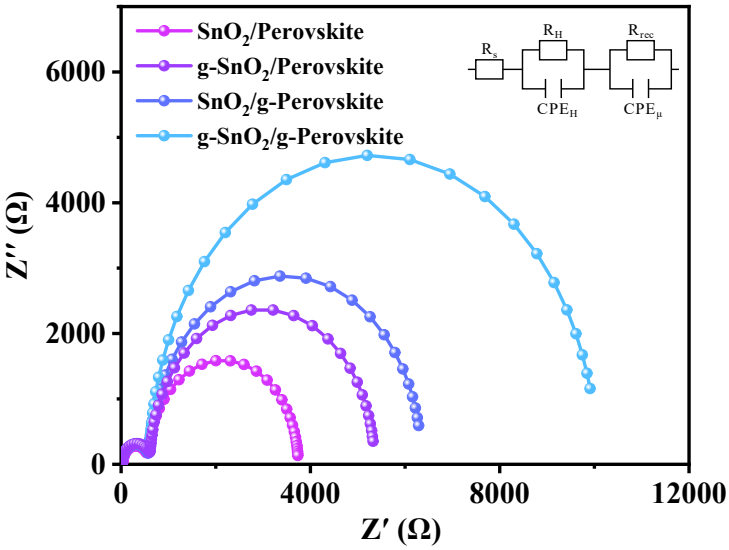

Figure S19. Nyquist plots of the PSCs were measured at 0.3 V in the dark, ranging from 10^6 to 10 Hz, including SnO_2/Perovskite, g-SnO_2/Perovskite, SnO_2/g-Perovskite, and g-SnO_2/g-Perovskite.

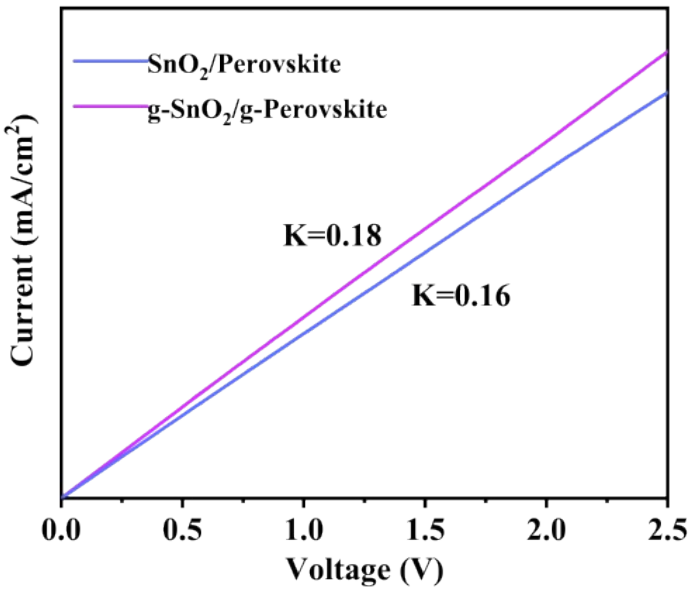

Figure S20. The conductivity measurement of SnO_2/perovskite and g-SnO_2/g-perovskite by using the space-charge-limited current (SCLC) model with a device structure of ITO/ETL/perovskite/Ag.

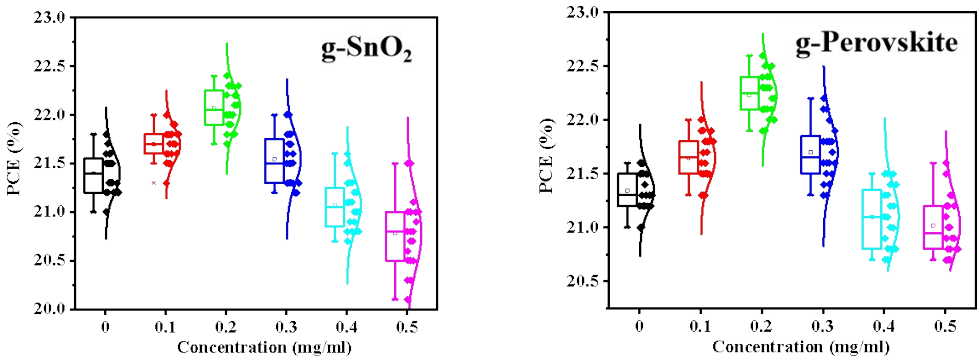

Figure S21. Histogram of devices with various g-C_3N_4 concentrations (0.1-0.5 mg/ml), respectively and histogram of devices with various g-C_3N_4 concentrations (0.1-0.5 mg/ml), respectively.

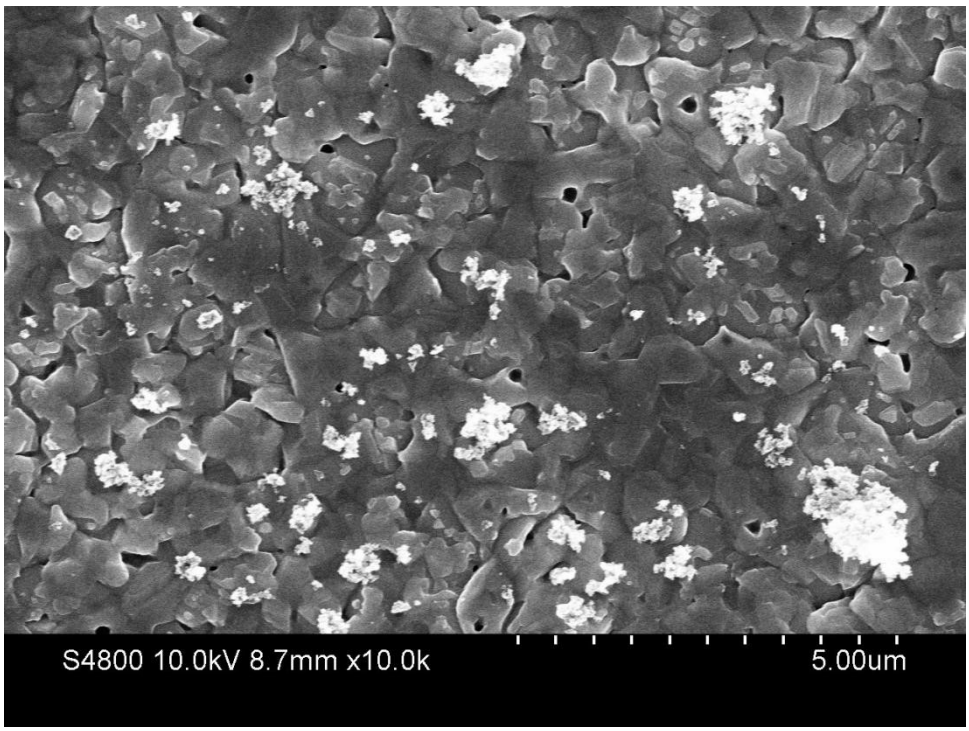

Figure S22. SEM images of the perovskite film with 5 mg/ml g-C_3N_4.

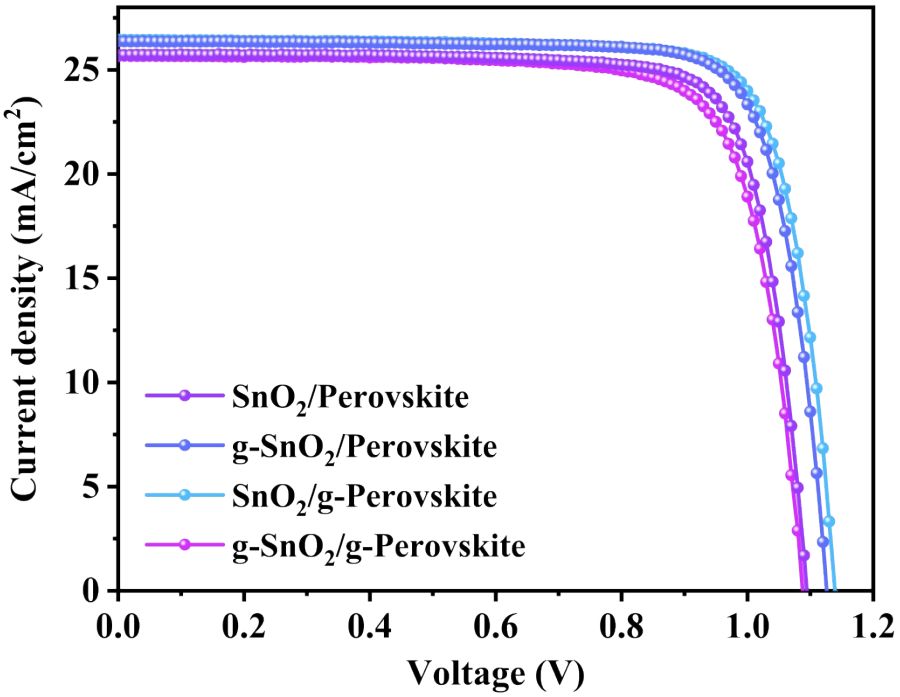

Figure S23. Optimized $J-V$ curves of the PSCs, including including SnO_2/Perovskite, g-SnO_2/Perovskite, SnO_2/g-Perovskite, and g-SnO_2/g-Perovskite.

Figure S24. EQE spectra with the integrated J_{sc} of the control and target devices.

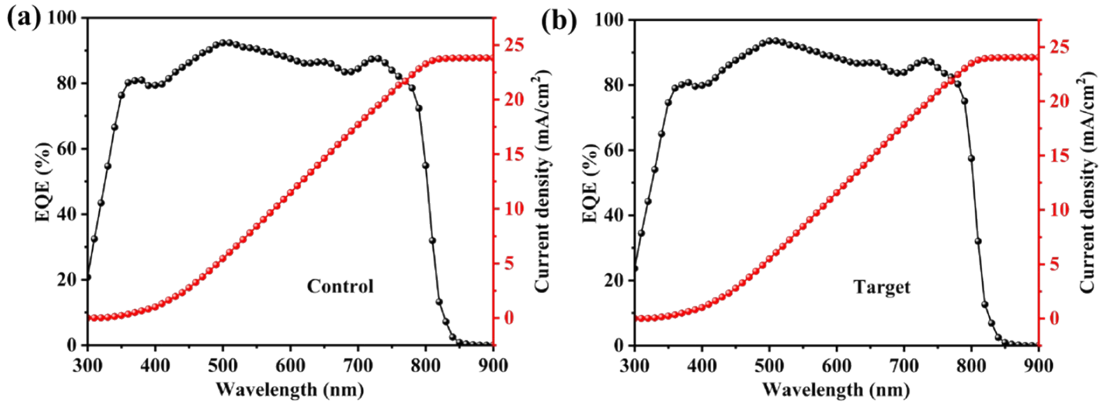

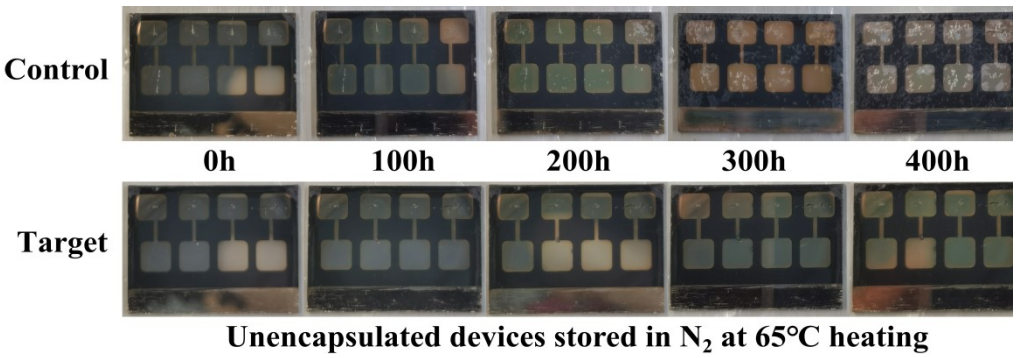

Figure S25. Temperature-dependent thermal stability of time for unencapsulated devices stored in N_2 at 65°C heating.

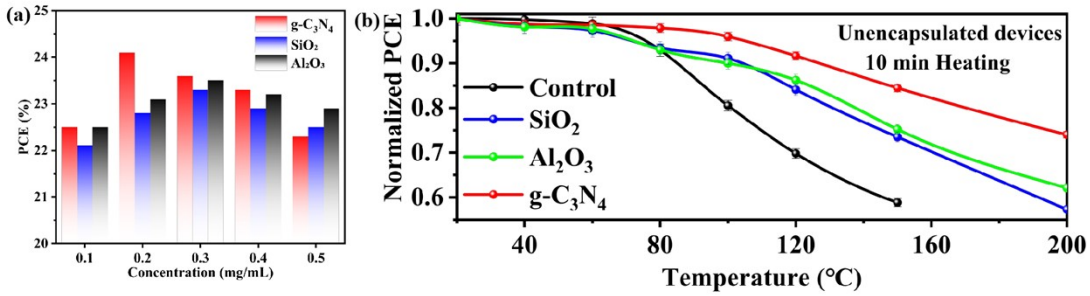

Figure S26. (a) Trend diagram of the PCE of PSCs based on different concentrations of additives, including g-C_3N_4, Al_2O_3 and SiO_2. (b) Normalized PCE for unencapsulated devices heated at different temperatures for 10 min including control, g-C_3N_4, Al_2O_3 and SiO_2.

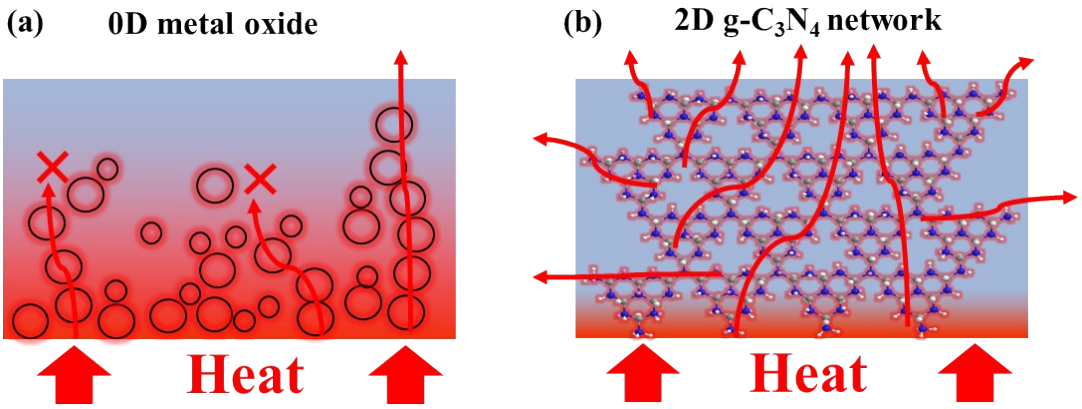

Figure S27. (a) Thermal transferring path diagram formed by a one-dimensional material Al_2O_3 and SiO_2 , and (b) the 3D thermal conduction path formed by g-C_3N_4.

Table S1. Fitted results of TRPL curves of the Control and Target films.

Samples	τ_1 (ns)	τ_2 (ns)	τ_{avg} (ns)
Control	28.03	137.93	103.41
Target	22.93	197.83	122.34

Table S2. EIS Parameters for the PSCs Based on the Control and Target.

Samples	R_s (Ω)	R_{rec} (Ω)
Control	31.85	3177
Target	13.81	9448

Table S3. Recent development of g–C_3N_4 based PSCs photovoltaic performance.

Structure	PCE (%)	Voc (V)	Jsc(mA ·cm^{-2})	FF (%)	Ref.
ITO/PTAA/NO_3-g-C_3N_4:CsFAMAPb$I_{3-x}Br_x$/PCBM/BCP/Ag	20.08	1.11	22.84	79.20	[1]
FTO/c-TiO_2/g-C_3N_4:$MAPbI_3$/spiro-OMeTAD /MoO_3/Ag	19.49	1.07	24.31	74.0	[2]
FTO/c-TiO_2/g-C_3N_4:$MAPbI_3$/spiro-OMeTAD /Au	21.10	1.16	23.00	79.0	[3]
FTO/c-TiO_2/m-TiO_2/g-C_3N_4:$CsPbBr_3$/carbon	8.00	1.277	7.80	80.32	[4]
FTO/c-TiO_2/m-TiO_2/Al_2O_3/g-C_3N_4:$MAPbI_3$/carbon	14.34	1.00	23.80	60.1	[5]
PDMS/hc-PEDOT:PSS/PEDOT:PSS/g-C_3N_4:$FASnI_3$/C60/BCP/Ag	8.56	0.621	20.68	66.68	[6]
FTO/TiO_2/G-CNI:CsFAMAPb$I_{3-x}Br_x$/spiro-OMeTAD/Au	18.28	1.07	22.97	74.0	[7]
FTO/c-TiO_2/U-g-C_3N_4:$MAPbI_3$/spiro-OMeTAD/Au	15.80	1.10	23.20	62.0	[8]
ITO/CNQDs:SnO_2/CsFAMAPb$I_{3-x}Br_x$/Spiro-OMeTAD/Au	22.13	1.18	24.03	78.3	[9]
FTO/SnO_2/CNQDs/(FA/MA/Cs)$PbI_{3-(x+y)}Br_xCl_y$/spiro-OMeTAD/Au	21.23	1.14	23.39	79.6	[10]
FTO/SnO_2/g-C3N4/$MAPbI_3$/g-C_3N_4/Sspiro-OMeTAD/Au	19.67	1.14	21.45	80.7	[11]

FTO/c-TiO_2/m-TiO_2/g-C_3N_4 nanosheets/$MAPbI_3$/ Carbon	11.37	1.02	16.91	66	[12]
FTO/c-TiO_2/g-C_3N_4/$MAPbI_3$/spiro-OMeTAD/Ag	19.55	1.11	23.69	74.0	[13]
ITO/g-C_3N_4:SnO_2/$FA_{0.85}MA_{0.11}Cs_{0.04}PbI_{2.67}Br_{0.33\cdot x}PbI_2$/spiro-OMeTAD/Au	21.54	1.19	23.21	78	[14]
ITO/PTAA/$MAPbI_3$/$PC_{60}BM$/CMB-vTA/AZO/Ag	17.15	1.09	20.17	78.03	[15]
FTO/TiO_2/thiazole-C_3N_4/$(FAPbI_3)_{0.875}(CsPbBr_3)_{0.125}$/spiro-OMeTAD/Ag	19.23	1.11	22.50	77	[16]
FTO/TiO_2/w-CN/$CsPbIBr_2$/w-CN/Carbon	10.1	1.36	11.19	66.39	[17]
ITO/PEDOT:PSS/g-C_3N_4QDs:$CsFAMAPbI_{3-x}Br_x$/PCBM/Ag	20.02	0.99	25.93	78	[18]
FTO/ZnO/TiO_2/g-C_3N_4/$MAPbI_3$/ Spiro-OMeTAD	20.57	1.11	24.03	77	[19]
ITO/g-C_3N_4:SnO_2/$FA_{0.93}MA_{0.07}PbI_3$:g-C_3N_4/spiro-OMeTAD/Ag	24.19	1.14	26.45	80.27	This study

References

[1] Li, Z.; Wu, S.; Zhang, J.; Yuan, Y.; Wang, Z.; Zhu, Z. Improving photovoltaic performance using perovskite/surface-modified graphitic carbon nitride heterojunction. *Sol. RRL* **2020**, *4* (3), 1900413.

[2] Jiang, L. L.; Wang, Z. K.; Li, M.; Zhang, C. C.; Ye, Q. Q.; Hu, K. H.; Lu, D. Z.; Fang, P. F.; Liao, L. S. Passivated perovskite crystallization via g-C_3N_4 for high-performance solar cells. *Adv. Funct. Mater.* **2018**, *28* (7), 1705875.

[3] Liao, J.-F.; Wu, W.-Q.; Zhong, J.-X.; Jiang, Y.; Wang, L.; Kuang, D.-B. Enhanced efficacy of defect passivation and charge extraction for efficient perovskite photovoltaics with a small open circuit voltage loss. *J. Mater. Chem. A* **2019**, *7* (15), 9025-9033.

[4] Liu, W.-W.; Liu, Y.-C.; Cui, C.-Y.; Niu, S.-T.; Niu, W.-J.; Liu, M.-C.; Liu, M.-J.; Gu, B.; Zhang, L.-Y.; Zhao, K. All-inorganic $CsPbBr_3$ perovskite solar cells with

enhanced efficiency by exploiting lone pair electrons via passivation of crystal boundary using carbon nitride (g-C_3N_4) nanosheets. *Mater. Today Energy* **2021**, *21*, 100782.

[5] Yang, Z.-L.; Zhang, Z.-Y.; Fan, W.-L.; Hu, C.-s.; Zhang, L.; Qi, J.-J. High-performance g-C_3N_4 added carbon-based perovskite solar cells insulated by Al_2O_3 layer. *Sol. Energy* **2019**, *193*, 859-865.

[6] Rao, L.; Meng, X.; Xiao, S.; Xing, Z.; Fu, Q.; Wang, H.; Gong, C.; Hu, T.; Hu, X.; Guo, R. Wearable tin-based perovskite solar cells achieved by a crystallographic size effect. *Angew. Chem. Int. Ed. Engl.* **2021**, *133* (26), 14814-14821.

[7] Cao, W.; Lin, K.; Li, J.; Qiu, L.; Dong, Y.; Wang, J.; Xia, D.; Fan, R.; Yang, Y. Iodine-doped graphite carbon nitride for enhancing photovoltaic device performance via passivation trap states of triple cation perovskite films. *J. Mater. Chem. C* **2019**, *7* (40), 12717-12724.

[8] Wei, X.; Liu, X.; Liu, H.; Yang, S.; Zeng, H.; Meng, F.; Lei, X.; Liu, J. Exfoliated graphitic carbon nitride self-recognizing $CH_3NH_3PbI_3$ grain boundaries by hydrogen bonding interaction for improved perovskite solar cells. *Sol. Energy* **2019**, *181*, 161-168.

[9] Chen, J.; Dong, H.; Zhang, L.; Li, J.; Jia, F.; Jiao, B.; Xu, J.; Hou, X.; Liu, J.; Wu, Z. Graphitic carbon nitride doped SnO_2 enabling efficient perovskite solar cells with PCEs exceeding 22%. *J. Mater. Chem. A* **2020**, *8* (5), 2644-2653.

[10] Liu, P.; Sun, Y.; Wang, S.; Zhang, H.; Gong, Y.; Li, F.; Shi, Y.; Du, Y.; Li, X.; Guo, S.-S. Two dimensional graphitic carbon nitride quantum dots modified perovskite solar cells and photodetectors with high performances. *J. Power Sources* **2020**, *451*, 227825.

[11] Liu, Z.; Wu, S.; Yang, X.; Zhou, Y.; Jin, J.; Sun, J.; Zhao, L.; Wang, S. The dual interfacial modification of 2D g-C_3N_4 for high-efficiency and stable planar perovskite solar cells. *Nanoscale Adv.* **2020**, *2* (11), 5396-5402.

[12] Jin, J.; Wu, S.; Yang, X.; Zhou, Y.; Li, Z.; Cao, Q.; Chi, B.; Li, J.; Zhao, L.; Wang, S. Improve the efficiency of perovskite solar cells through the interface modification of g-C_3N_4 nanosheets. *Mater. Lett.* **2021**, *304*, 130685.

[13] Yang, J.; Chu, L.; Hu, R.; Liu, W.; Liu, N.; Ma, Y.; Ahmad, W.; Li, X. a. Work function engineering to enhance open-circuit voltage in planar perovskite solar cells by g-C_3N_4 nanosheets. *Nano Res.* **2021**, *14*, 2139-2144.

[14] Yang, X.; Li, L.; Wu, J.; Hu, Q.; Wang, Y.; Russell, T. P.; Tu, Y.; Zhu, R. Optimizing vertical crystallization for efficient perovskite solar cells by buried composite layers. *Sol. RRL* **2021**, *5* (10), 2100457.

[15] Wang, L.; Fu, L.; Li, B.; Li, H.; Pan, L.; Chang, B.; Yin, L. Thiazole-Modified C_3N_4 Interfacial Layer for Defect Passivation and Charge Transport Promotion in Perovskite Solar Cells. *Sol. RRL* **2021**, *5* (3), 2000720.

[16] Cruz, D.; Garcia Cerrillo, J.; Kumru, B.; Li, N.; Dario Perea, J.; Schmidt, B. V.; Lauermann, I.; Brabec, C. J.; Antonietti, M. Influence of thiazole-modified carbon nitride nanosheets with feasible electronic properties on inverted perovskite solar cells. *J. Am. Chem. Soc.* **2019**, *141* (31), 12322-12328.

[17] Shi, L.; Yuan, H.; Zhang, Y.; Sun, X.; Duan, L.; Li, Q.; Huang, Z.; Ban, X.; Zhang, D. Novel C_3N_4-assisted bilateral interface engineering for efficient and stable perovskite solar cells. *Langmuir* **2022**, *38* (40), 12390-12398.

[18] Jiang, L.-L.; Chen, M.-M.; Tang, X.-D.; Tang, Y.; Li, S.-J.; Li, Y.; Li, H.-H.; Liu, H.-R. Reduced electron relaxation time of perovskite films via g-C_3N_4 quantum dot doping for high-performance perovskite solar cells. *RSC advances* **2023**, *13* (25), 16935-16942.

[19] Gkini, K.; Martinaiou, I.; Botzakaki, M.; Tsipas, P.; Theofylaktos, L.; Dimoulas, A.; Katsaros, F.; Stergiopoulos, T.; Krontiras, C.; Georga, S. Energy band tuning induced by g-C_3N_4 interface engineering for efficient and stable perovskite solar cells. *Mater. Today Commun.* **2022**, *32*, 103899.